[00050] Fig. 17: Electric dipoles in (a) 21 helical PHB chains (α-form) and (b) planar zig-zag PHB chains (β-form).

[00051] Fig. 18: Electric charge movements during a press-hold-release cycle. The black line represents the real voltage signal. The dark green line represents the free charge transport from the external circuit to the fibers. The pink line represents the net charges in the ribbon of fibers.

[00052] Fig. 19: (a) Schematic illustration of an analytical model for the response of the PHBHx ribbon of fibers under applied pressure. The blue letter p and red letter A denote the applied pressure and the contact area of the probe and the ribbon of fibers, respectively. (b) Experimental (black) and linear fitted (red) pressure response curves

[00053] Fig. 20: WAXD profile of neat, annealed 3.9 (a) and 13 (b) mol % 3HHx PHBHx films and stretched (c) 13 mol % 3HHx PHBHx film oriented with X-ray beam perpendicular to stretching direction.

[00054] Fig. 21: IR spectra of neat 13 mol % 3HHx PHBHx polymer film as a function of increasing strain.

[00055] Fig. 22: Raman spectra of neat 13 mol % 3HHx PHBHx polymer film before and after strain.

[00056] Fig. 23: Raman spectra of neat 13 mol % 3HHx PHBHx polymer film before and after strain focused on the carbonyl region.

[00057] Fig. 24: Stretched film showing unstretched α and stretched β regions.

[00058] Fig. 25: XRD of amorphous, unstretched α region, and stretched β region of same film.

[00059] Fig. 26: XRD spectrum of a film after stretching and being released

[00060] Fig. 27: XRD spectrum of film after being stretched, released, and had tension restored.

[00061] Fig. 28: XRD as a function of strain.

[00062] Fig. 29: XRD spectrum of stretched film annealed for 2 hours at 48℃.

[00063] Fig. 30: XRD spectrum of stretched films after isothermal crystallization at room temperature

[00064] Fig. 31: Raman spectrum of stretched films after isothermal crystallization at room temperature.

[00065] Fig. 32: Thermally reversible sol-gel transition in PHBHx $CHCl_3$/DMF solution.

[00066] Fig. 33: WAXD profiles of (a) raw PHBHx powder and (b) freeze-dried gel.

[00067] Fig. 34: WAXD profiles of the gel film (a) before and (b) after stretching.

amount of from 1-99% or 5-90% or 10-80%, based on the total weight of the solution. Any suitable solvent may be used, including but not limited to**,** chloroform, toluene, acetone, and the like**.** The layer can be formed using any suitable method such as, casting.

[00097] In another embodiment of the process, the step of providing a layer comprises forming a layer from a melted composition of the polyhydroxyalkanoate based copolymer and the step of directionally perturbing the layer comprises calendar rolling, shearing or cold drawing the layer after quenching.

[00098] In an embodiment of the process, the step of providing a layer comprises forming a film from a gel composition of the polyhydroxyalkanoate based copolymer and the step of directionally perturbing the film comprises drying gel under shear pressure or freezing gel to induce shear by crystallization of solvent. The gel composition of the polyhydroxyalkanoate based copolymer can be formed by any suitable method, such as disclosed hereinbelow in Example 6**.**

[00099] In an embodiment of the process, the polyhydroxyalkanoate based copolymer comprises at least one monomer unit selected from the group consisting of hydroxybutyrate units, hydroxyhexanoate units, vinyl units, vinylidene units, ethylene units, acrylate units, methacrylate units, Nylon units, carbonate units, acrylonitrile units, cellulose units, units having pendant fluoro, chloro, amide, ester other than ester of acrylate and methacrylate units, cyanide, nitrile other than of acrylonitrile units, or ether groups, protein units and combinations thereof.

[000100] In another embodiment of the process, the polarizable polymeric composition further comprises one or more polymers selected from the group consisting of polyvinylchloride, polymethylacrylate, polymethylmethacrylate, poly(vinylidene cyanide/vinyl acetate) copolymers, vinylidene cyanide/vinyl benzoate copolymers, vinylidene cyanide/isobutylene copolymers, vinylidene cyanide/methyl methacrylate copolymers, vinylidene fluoride copolymer, polyvinylfluoride, polyacrylonitrile, polycarbonate, cellulose, proteins, synthetic polyesters and ethers of cellulose, poly(gamma-methyl-L-glutamate), vinylidene copolymers, Nylon-3, Nylon-5, Nylon-7, Nylon-9, Nylon-11 and blends thereof.

[000101] In an aspect of the process, the layer comprises at least two layers of the polarizable polymeric composition formed from a multiphase composition of said polymer composition. In an embodiment, the at least two layers are co-extruded and are in contact with one another.

[000102] In an embodiment of the process, the step optionally polarizing the polymeric composition of the directionally perturbed layer is conducted using an electric field of at least 1 MV/cm at a temperature from about 20° C. to about 120° C. for up to

exhibited the smallest ψ for all arcs, suggesting that in this single fiber the α-form crystals had the highest degree of orientation among the three samples, and the polymeric chains in the crystals were highly oriented along the fiber axis. The crystalline reflection of the β-form crystals appeared in fibers from the two modified collectors where a pair of new equatorial arcs were observed in both 4b' and 4c', which are assigned to the β-form crystal plane. Since the β-form crystal structure is a strain-induced paracrystalline structure, this observation indicates that the two modified collectors indeed introduced extra stretching forces on the fibers which are strong enough to stretch the polymer chains to an essentially fully extended form. It is also noted that the β-form arcs always had a small central angle of 8° (Table 2), suggesting a high orientation of the molecular chains in the β-crystals along the fiber axis under different collection conditions.

[000155] Table 2. Schematic of the SAED Patterns of Single Fibers Collected with Different Methods and Central Angles of the Arc Reflections of the Indexed Crystalline Planes

		Collector		
		Al foil	Air gap	Rotary disk
Schematic reflection pattern [a]		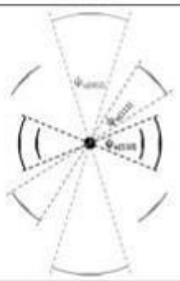	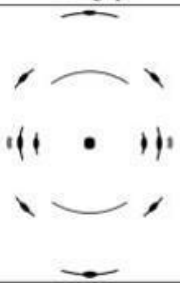	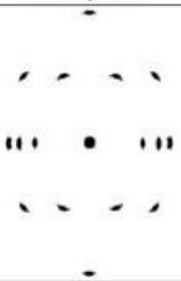
Central angle (ψ°)	α(020)	31	23	11
	α(110)	37	25	12
	α(111)	22	16	12
	α(002)	30	24	8
	β-form	-	8	8
SAED intensity profiles		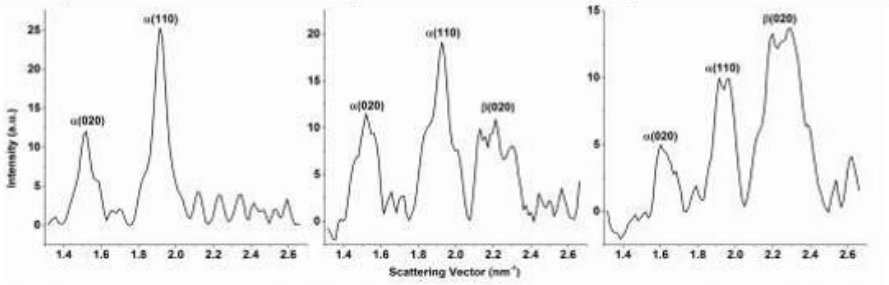		

[a] The intensities of the reflections are represented by the gray scale.

[000156] For each of the three SAED patterns, the intensity profile along the equatorial line was plotted against the scattering vector (1/*d*, reciprocal of space distance), and the profiles obtained are shown in Table 2. In order to eliminate the influence of nonstructure-related factors, such as electron beam conditions and photorecording conditions, the background gray values for all three SAED patterns were equalized before analysis. The baseline was corrected by fitting the background for each of the profiles. The following observations were made from these intensity profiles, first, from left to right, the intensities of the α(020) and α(110) peaks both decreased while the intensity of the β peak increased, indicating a decrease in the α-crystal structure content and a correlated increase in the β-crystal structure content. These observations indicate that the stretching forces from the insulated gap, which are caused by the electrostatic attraction between the positively charged fibers and the negatively charged gap edges and the electrostatic repulsion between the residual positive charges on each fiber, are significantly weaker than those from the rotary disk. In addition, the correlated increase of the β-crystal content along with the decrease of

speed rotary disk. Current results suggest that under this specific electrospinning condition the appearance of the β-crystalline phase is indicated by the characteristic IR absorption peak at 1740 cm^{-1} in the IR spectrum. The IR absorption peak at 1728 cm^{-1} is characteristic of the α-crystalline phase, which is the thermodynamically stable crystal structure of PHBHx. In order to investigate the spatial distribution of the two crystalline phases in the nanofibers, the two single fibers were imaged by tuning the frequency of the incident IR laser to 1740 and 1728 cm^{-1}, the two characteristic frequencies corresponding to the βform and α-form crystalline structure, respectively. The IR images are shown in Figures 8b and 8b'. For each IR image, the upper half was recorded at 1740 cm^{-1} and the lower half at 1728 cm^{-1}. By carefully examining these IR images, one can make several observations. First, when comparing Figures 8b and 8b', it is observed that both fibers have detectable IR absorption at 1740 and 1728 cm^{-1}, indicating the coexistence of the α- and β-crystalline phase at the single fiber scale. In addition, under the same mapping conditions, the thinner fiber (263 nm) has higher absorption at 1740 cm^{-1} yet lower absorption at 1728 cm^{-1}, indicating that the thinner fiber tends to have higher β-content than the thicker fiber (390 nm). Because the two fibers were fabricated under the same electrospinning conditions, the difference in diameter should be due to the different stretching forces they experienced during electrospinning and collection. Assuming extensional strain, the draw ratio of the 263 nm fiber is approximately 2.2 times larger than that of the 390 nm fiber. Since a higher draw ratio favors an extended chain, more molecular chains in the thinner fiber would be found in the planar zigzag conformation and pack to form the β-crystalline form.

[000179] The coexistence of both α- and β-form crystal structures in single PHBHx nanofibers as well as the dependence of the β-form content on fiber diameter is reaffirmed by the SAED patterns of individual PHBHx nanofibers. Figures 9a and 9a' display the original SAED patterns of two single PHBHx nanofibers from the same batch. The insets show the brightfield TEM images of the two single fibers. The diameters of the two fibers are 251 and 417 nm, respectively, which are comparable with those of the two fibers in the AFM-IR study. For comparative purposes, the original SAED patterns were contrast-inverted as shown in Figures 9b and 9b'. By comparing the two inverted SAED patterns, it is observed that the equatorial arcs assigned to the β-form crystal plane14 are clearly visible in Figure 9b (indicated by the red arrow), while in Figure 9b' they can barely be recognized. For each of the SAED patterns, the intensity profile along the equatorial line was plotted in Figures 9c and 9c' correspondingly against the scattering vector (1/d, reciprocal of space distance). Obviously, the intensity of the β-peak in Figure 9c is much higher than that in Figures

intensities of the highest peaks of all spectra were normalized to 1.0. By comparing C1 and C1′, it was observed that both spectra have characteristic peaks at 1728 and 1740 cm^{-1}, although the 1740 cm^{-1} peak in C1 has a much higher intensity than that in C1′, indicating that through the core area the 263 nm diameter fiber has more β crystalline content than the 390 nm diameter fiber. By comparing the color paired two groups of curves, i.e., C1, E1 (solid spectra) and C1′, E1′ (dashed spectra), it should be noticed that E1 and E1′ always tend to have a much higher 1740 cm^{-1} peak compared to C1 and C1′. This observation indicates that the morphology of the polymer chains indeed shows heterogeneity throughout a single fiber, and the shell contains more β-form crystals than the core. Interestingly, when comparing E1 and E1′, there is not much difference between the two spectra in terms of band shape, which suggests that the crystal structure or the chain morphology in the shell is independent of fiber size.

[000183] Additional support for the conclusion that the rotary disk aligned, electrospun PHBHx nanofibers have a core−shell structure comes from an investigation of the cross sections of the fibers. Figures 11a and 11a′ show the AFM height image of the cross sections of two rotary disk aligned fibers from the same batch with diameters of 260 and 312 nm, respectively. Again, IR images were captured at the two characteristic frequencies of 1740 and 1728 cm^{-1}. In order to eliminate the influence of sample thickness variation and thermal drift, the ratio of the two mappings, i.e. I_{1740}/I_{1728}, was taken as shown in Figures 11b and 11b′. The color bar indicates the increase of the relative intensity of the IR absorption from purple to red. Since the 2 Ton epoxy has negligible absorption of the IR laser at 1740 and 1728 cm^{-1}, the IR mapping ratio in the epoxy area should equal 1, which is represented by the green/yellow color in Figures 11b and 11b′. As shown, for each of the two fiber cross sections, a clear red ring was observed at the circumference of the fiber cross section, making a clear differentiation of the fiber cross section and the epoxy. This indicates that in the ring area the ratio of I_{1740}/I_{1728} is larger than 1, or the IR absorption at 1740 cm^{-1} is higher than that at 1728 cm^{-1}. This observation confirms the existence of a thin shell, which contains more β-form crystals, in the rotary disk aligned electrospun PHBHx nanofibers. Furthermore, for both of the cross sections, the thickness of the ring is consistently found to be approximately 10 nm, which is comparable with the width of the red lines along the fiber edges in Figures 8b and 8b′. This strongly suggests that the thickness of the shell in the fibers is about 10 nm, regardless of the fiber diameter. In addition, it is also observed that in Figure 11b the color in the core area of the fiber cross section is yellow, which shifts toward the red direction compared to the green color in the epoxy area. This indicates a slightly higher content of β-form than the α-form in the core.

rectangular stainless steel layer. PZT sheet A at the top has a dimension of 22 mm (length) x 3.5 mm (width), while sheet B at the bottom is slightly shorter with a dimension of 12 mm x 3.5mm. A thin brass cylinder with a diameter of 1 mm was glued to the tip of the cantilever to act as the testing probe. More details about the piezoelectric cantilever can be found elsewhere. Due to a converse piezoelectric effect, the application of external voltages across the PZT sheet A will generate axial displacement of the cantilever, as well as the testing probe. Figure 13(b) shows the displacement of the probe at different applied voltages. The probe displacement was measured using a laser displacement sensor (LC-2450, Keynece Corporation) with a resolution of 0.5 μm. The external voltage was supplied by a function generator (Agilent 33220A, 20MHz).

[000198] For measuring the piezoelectric response of the fibers, a 5 mm wide × 10 mm long ribbon of fibers was interfaced with a flexible PDMS substrate. In order to reduce the background noise, this PDMS substrate was covered with insulating Kapton® tape. Conductive copper tape (3M 3313, 1/2 inch), serving as the electrodes, was used to stick the two ends of the ribbon of fibers onto the substrate in a way such that the aligned fibers are completely straight without load. The piezoelectric test started with a careful engagement of the cantilever probe onto the surface of the ribbon of fibers, Square wave voltages, supplied by the function generator, were applied across the cantilever to generate the vibration of the cantilever at a frequency of 10 Hz. The probe, in contact with the ribbon of fibers, thus deformed the straight fibers synchronously. The induced voltages resulting from the deformation of the aligned fibers were recorded on a digital oscilloscope (Agilent Infinitum 1.5 GHz, 8GSa/s). The experimental set-up is illustrated in Figure 14. Control experiments were performed to verify that no obvious voltage signal was observed without the ribbon of fibers. All experiments were performed on a Newport optical table (RS100, Newport Corporation) to minimize background vibrations.

[000199] **Results and Discussion**

[000200] The morphologies and crystal structures in macroscopically aligned PHBHx nanofiber bundles before and after annealing are shown in Figure 15. It is observed that after annealing, the macroscopic alignment of the fibers remained constant. The β-form crystals disappeared, presumably by conversion to the thermodynamically stable α-form, as demonstrated by the loss of the X-ray diffraction peak of the β-form at 19.6° shown in Figure 15b'. Furthermore, the two diffraction peaks of the α-form became narrower, i.e. the FWHM of the two α-peaks became smaller after annealing, indicating that the size of the α-crystals increased due to the reorganization of the molecular chains during annealing.

[000201] The piezoelectric response of the PHBHx nanofibers before and after annealing was measured with an applied voltage of 10V. The results are presented in Figure 16. Quantitatively, the fibers before annealing (signal in black) exhibit a much higher voltage output (c.a. 240 mV peak to peak) than the fibers after annealing (signal in red), indicating a strong correlation of the piezoelectricity of the fibers with the presence of the β-form crystal structure.

[000202] The β-crystalline form contains molecular chains that exhibit a planar zig-zag conformation. As shown in Figure 17b, the electronegative O atoms from the C=O group and the electropositive H atoms from the adjacent CH2 group reside on opposite sides of the polymer backbone. As a result, a net dipole moment is formed perpendicular to the polymer backbone. Previous studies showed that the polymer chains in the rotary disk aligned fibers are highly oriented along the fiber axis. Therefore, when aligned fibers are bent, the oriented polymer chains confined in the fibers are deformed, which causes a change of the dipole moment. Consequently, a potential difference is generated between the two ends of the fibers, which appears as the positive black voltage spikes in Figure 16. On the other hand, although electric dipoles exist in the molecular chains of the α-form, the left-handed 21 helical conformation aligns all the dipole moments in a way that they cancel each other (Figure 17a). This results in a zero net dipole moment in the α-crystals, and thus the annealed aligned fibers containing only the α-form crystalline structure exhibit no piezoelectric response. Interestingly, Ando and his co-workers18–20 investigated the piezoelectric properties of α-PHB and found that oriented α-form PHB exhibits intrinsic shear piezoelectricity. The internal rotation of dipolar atomic groups associated with the asymmetric carbon atoms (O=C-CH2, Figure 17a) in the helical chains of the α-form seem to cause electric polarization when shear stress is applied. However, this shear piezoelectricity was not observed in Figure 16. This difference might be due to: (1) the molecular chains are not sufficiently sheared in this experiment to display the shear piezoelectricity, since the shear piezoelectric coefficient of α-PHB is low; or (2) the annealing process may have degraded the high orientation level of the chains, so the α-crystals after annealing are randomly distributed in the fibers. Further investigations are necessary to gain a better insight into this observation.

[000203] Another interesting feature in Figure 16 is the alternative appearance of positive and negative voltage spikes. This phenomenon can be explained by the charge and discharge of the piezoelectric PHBHx fibers during the press-hold-release cycle (Figure 18). When the brass probe starts to press the ribbon of fibers, the oriented molecular chains in the fibers are deformed, which results in an

instantaneous potential difference between the two ends of the ribbon of fibers. Quantitatively, this potential difference is represented by the positive voltage signal of 119 millivolts in Figure 18. In response to this induced potential difference, external free charges (green line) are driven to the ribbon of fibers to neutralize this potential difference. During this process, the net charge (pink line) on the ribbon of fibers increases. When the press is held, i.e. the mechanical strain remains constant, both the induced potential difference and the net charge are gradually diminished, as the piezoelectric bound charges are balanced by the external free charges. At zero potential difference, the ribbon of fibers is fully charged. When the press is released, the built-in potential difference disappears, and the external free charges accumulated at both ends of the ribbon of fibers flow back in a direction opposite to the accumulation process. This reversal results in a quantitative opposite potential difference (-123 millivolts) which is observed as the negative voltage signal. As shown in Figure 18, the opposite potential difference and net charge also experience a gradual reduction. As soon as the potential difference reaches zero, the discharge of the ribbon of fibers is complete.

[000204] The above experimental results suggest the possibility of using piezoelectric PHBHx nanofibers as nanogenerators. Meanwhile, the piezoelectric characteristics make the ribbon of fibers promising building blocks for piezoelectric sensors. In order to evaluate the sensitivity of the ribbon of fibers, the applied voltage was adjusted to explore the relationship between the induced voltage and the applied pressure using the apparatus shown in Figure 19. The pressure applied on the fibers is calculated by the equation:

$$p=(K\times D)/A$$

where K represent the spring constant of the cantilever, D is the axial displacement of the probe, and A is the contact area of the probe with the ribbon of fibers. It is known that K=128.9±2.2 N/m22.

[000205] D is measured by the laser displacement sensor as shown in Figure 19a and A= πr2 where r=0.5 mm. The induced voltages were recorded through a range of applied voltages from 4 to 10 V with increments of 1 V. A plot of the induced voltage as a function of the applied pressure is shown in Figure 19b, and a linear relationship was observed. Hence, the sensitivity of the ribbon of fibers can be calculated from the slope of the linear fit, which turns out to be 7.46 mV/kPa. Although this sensitivity seems to be much low compared to other piezoelectric sensors, it can be improved by methods including: 1) changing the sensor architecture, e.g., stacking multiple layers of piezoelectric ribbon of fibers together; or 2) increasing the concentration of the piezoelectric-active component (β-crystals) in the fibers.

[000206] **Conclusions**

[000207] In this study, the piezoelectric properties of the electrospun PHBHx nanofibers were investigated as a function of crystal structure. The piezoelectric response of the rotary disk aligned fibers, before and after annealing, was characterized. The results showed that nanofibers containing the metastable β-form crystalline structure consisting of planar zig-zag chains, exhibit an obvious piezoelectric response (240 millivolts peak-to-peak) when mechanically deformed. However, after annealing and conversion of the β-form crystals to the α polymorph this piezoelectric response disappeared. This observation indicated a strong correlation between the piezoelectric properties of the fibers and the presence of the β-form crystalline structure. Subsequently, the sensitivity of the piezoelectric PHBHx nanofibers to the applied pressure was measured. The induced voltages were recorded as the applied pressure was changed and a linear relationship was observed. From the slope, a piezoelectric sensitivity for the fibers was measured to be 7.46 mV/kPa. The implications of these preliminary investigations of the piezoelectricity of PHBHx are far reaching. Piezoelectric performance of this material can be significantly improved by increasing the concentration of the active β-form crystalline structure. That goal can be accomplished by utilizing innovative polymer processing techniques, such as those discussed herein. The piezoelectric PHBHx distinguishes itself from all the other piezoelectric polymers with its excellent biodegradability and biocompatibility, environmental-friendliness and most importantly, low manufacturing cost. It is a very promising piezoelectric polymer that may find applications in many advanced areas including portable and foldable electronic devices, artificial electronic skin and implantable sensors.

[000208] **Example 4: Stress-induced Beta Crystallization of Poly[(R)-3-hydroxybutyrate-*co*-(R)-3-hydroxyhexanoate] in FILMS**

[000209] **Materials**

[000210] Poly[(R)-3-hydroxybutyrate-co-(R)-3-hydroxyhexanoate] (PHBHx) copolymers with 3.9 and 13 mol % 3HHx comonomer content were supplied by the Procter & Gamble Company, Cincinnati, Ohio with no further purification. The weight average molecular weight of the 3.9 and 13 mol % 3HHx copolymers were 843 and 792 kg/mole, respectively. Chloroform was purchased from Sigma-Aldrich Co., Ltd and used without further purification.

[000211] **Sample Preparation**

[000212] Films of PHBHx were prepared by dissolving the polymer in chloroform and solvent casting the film on a Teflon block to avoid binding to the casting surface.

profile for comparison with the alpha form. Additionally, in highly oriented samples, the majority of the alpha diffraction peaks tend to go unobserved in one-dimensional diffraction studies, due to the crystal orientation in the sample. Figure 20 contains the diffraction profile of neat 3.9 and 13 mol % 3HHx PHBHx polymer films after annealing and 13 mol % 3HHx PHBHx polymer film after strain was applied. The 3.9 mol % 3HHx PHBHx annealed film was included in the study to demonstrate the number of alpha crystal diffraction peaks for comparison to the stretched film.

[000222] 3.9 mol % 3HHx PHBHx WAXD profile contains the three diffraction peaks listed previously, in addition to another alpha peak at ~19.5 2θ while the 13 mol % 3HHx PHBHx annealed film includes the alpha (020) and (110) peaks in addition to a broad peak centered at 21.5 2θ. The stretched film WAXD profile also contains the alpha (020) and (110) peaks, but shows an additional large, broad peak centered at 19.5 2θ. This broad diffraction peak is typical of a PHA sample containing beta form. Notice, however, that the higher 2θ diffraction peaks of the alpha crystal are nearly unobservable. The lack of diffraction from the other crystal planes is due to the high amount of orientation that was introduced into the sample during the two step stretching. Because the sample is oriented in the XRD with the stretching direction perpendicular to the X-ray beam, the alpha crystal lamella are oriented with the c axis parallel to the stretching direction. Additionally, the beta form is also oriented with the c axis parallel to the stretching direction. A comparison to the other diffraction profiles Figure 20 illustrates the issue with using XRD to confirm the presence of the beta form. In the same position as the maximum of the beta peak is a diffraction peak arising from the alpha form, seen in the 3.9 mol % 3HHx PHBHx film. If a sample is oriented a certain way with respect to the X-ray beam path, this peak could increase in relative intensity and give the illusion of beta form, especially if the alpha crystals are small in diameter, which causes the diffraction peaks to broaden. Overall, these profiles strongly suggest that the beta form was produced in the stretched film, but further analysis was required.

[000223] To confirm the presence of the beta form in the stretched films of 13 mol% 3HHx PHBHx, IR spectra were taken as the film was stretched at room temperature after the first strain was applied below Tg. These spectra only contain the backbone region because the films were too thick, causing over-absorbance of the carbonyl. Thinner samples were not mechanically stable enough for use in the mechanical stretching device. Figure 21 contains the IR spectra of neat 13 mol % 3HHx PHBHx polymer film as a function of increasing strain.

[000224] Based on the presence and consistency of the bands at 1278, 1263, and 1228 cm^{-1}, all of which are assigned to the helical conformation, the polymer

be seen in Figure 27 in a film that has been stretched, released, and had tension immediately restored, respectively. In addition to the XRD spectrum, a Raman spectrum of the released film was obtained to be sure that the β conformation had disappeared.

[000240] This was not the case when re-stretching the released films that had been left at room temperature for 24 hours. As seen in Figure 28, the β content gradually increased as the elongation increased. Due to the increased crystallization, when the film was re-stretched, the necked area continued to stretch more and more as the film was elongated. The surrounding non-necked regions were too crystalline and rigid to become necked, so the already necked region continued to elongate. It can be seen that the peaks associated with the α crystal structure decrease in size before the peak associated with the β structure increase. The size of the α crystalline domains also seems to decrease slightly, although this is less prominent than the overall decrease in the height of the peaks. This shows that when the film is re-stretched, the α crystals melt first into an intermediate state and then form the β structure.

[000241] It is clear that the β conformation did not remain after tension was released.

[000242] Additional annealing was done at 48℃ for 2 hours. An XRD spectrum of this film is shown in Figure 29. The α content of the stretched film increases significantly as a result of this treatment. Additionally, the amount of β conformation decreased as a result of the annealing. Upon being released, it seems that a small amount of β conformation may remain. However, this film was taped to the XRD sample holder, and it is possible that this process put slight tension on the film, restoring the β conformation.

[000243] To optimize the formation of the β conformation, films were left to isothermally crystalize for differing amounts of time before being stretched. Films were stretched after 25, 28, 30, 35, and 40 minutes. When stretched after 25 minutes of crystallization, the entire film elongated over 200% without signs of breaking. The stretched films after 25 and 28 minutes of crystallization were analyzed using XRD and Raman, seen in Figures 30 and 31, respectively.

[000244] The above spectra show that the film stretched after 25 minutes of crystallization did not form any β conformation, while the film stretched after 28 minutes did form a large amount of the β conformation.

[000245] It has been shown in this example that isothermal crystallization of 13 mole percent Hx in PHBHx films at room temperature can form the β conformation using a single stretch. However, the XRD peak for this conformation is broad, and it is

[000257] While preferred embodiments of the invention have been shown and described herein, it will be understood that such embodiments are provided by way of example only. Numerous variations, changes and substitutions will occur to those skilled in the art without departing from the spirit of the invention. Accordingly, it is intended that the appended claims cover all such variations as fall within the spirit and scope of the invention.

[000258] **Example 7: Method of making poled PHA copolymer based articles**

[000259] Five parts of PHBHx3.9 powder are dissolved in 95 parts chloroform ($CHCl_3$) at 100 - 125 degrees centigrade and the solution is transferred to a tray and put in a vacuum oven. Oven is maintained at 10-3 torr and a temperature range within 120 – 140 degrees C until a PHBHx solution is obtained having approximately 80% PHBHx3.9 by weight and 20% DMF by weight. The PHBHx3.9 solution is transferred as a film to a press subjected to a pressure of 3000 PSI and heated to various temperatures ranging from 95 – 125 °C. The film is then rapidly cooled in an ice bath. The film is then transferred to a poling apparatus consisting of two polished copper plates, which are in turn connected to a high voltage DC power supply. The temperature of the film is raised to slightly above the melting point and the film is poled. In one embodiment, during the poling, the temperature is decreased linearly at 2 d°C/min to 30 °C/min and the poling field I increased linearly from 25KV/cm to 1000 KV/cm. At room temperature the poling field is reduced to zero.